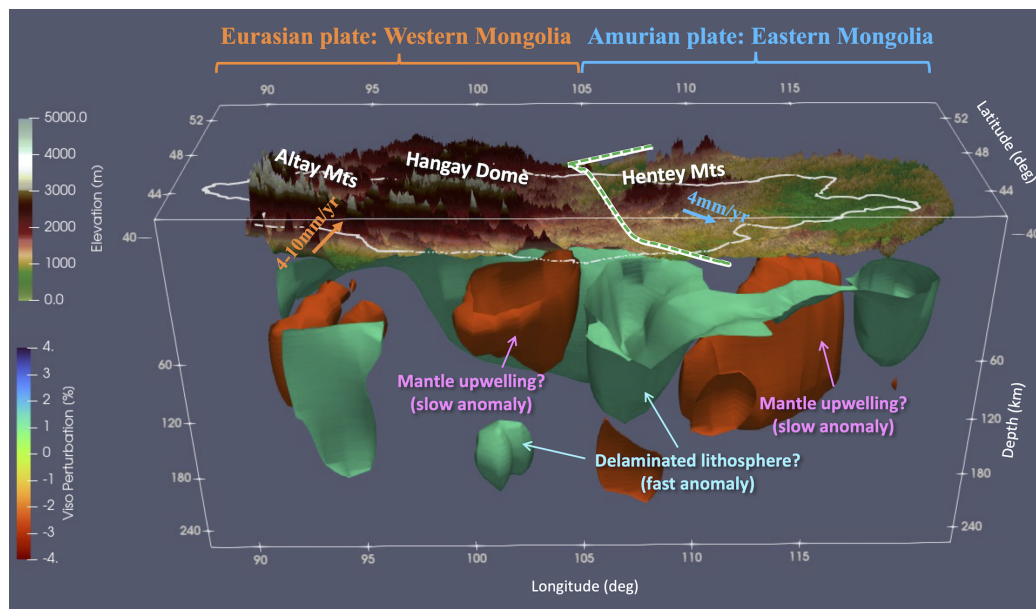


1 Graphical Abstract

2 Upper mantle structure beneath the Mongolian region from multi- 3 mode surface waves: Implications for the western margin of Amurian 4 plate

5 Baigalimaa Ganbat, Kazunori Yoshizawa, Demberel Sodnomsambuu, Ulzi-
6 ibat Munkhuu



7 Highlights

8 **Upper mantle structure beneath the Mongolian region from multi-** 9 **mode surface waves: Implications for the western margin of Amurian** 10 **plate**

11 Baigalimaa Ganbat, Kazunori Yoshizawa, Demberel Sodnomsambuu, Ulzi-
12 ibat Munkhuu

- 13 • Multi-mode surface waves are used to build a new 3-D Mongolian upper
14 mantle model.
- 15 • Significant velocity contrast is found beneath the Eurasian-Amurian
16 plate boundary.
- 17 • Anomalous structures are found beneath the Hangay Dome uplift and
18 the Amurian plate.

19 Upper mantle structure beneath the Mongolian region
20 from multi-mode surface waves: Implications for the
21 western margin of Amurian plate

22 Baigalimaa Ganbat^{a,c}, Kazunori Yoshizawa^{a,b}, Demberel Sodnomsambuu^c,
23 Ulziibat Munkhuu^c

*^aDepartment of Natural History Sciences, Graduate School of Science, Hokkaido
University, Sapporo, 060-0810, Japan*

*^bDepartment of Earth and Planetary Sciences, Faculty of Science, Hokkaido
University, Sapporo, 060-0810, Japan*

*^cInstitute of Astronomy and Geophysics, Mongolian Academy of
Sciences, Ulaanbaatar, 13343, Mongolia*

24 **Abstract**

25 Multi-mode phase speeds of surface waves are used to build a new radially
26 anisotropic S wave model in the middle Eurasian and Mongolian regions. Our
27 dataset includes seismic waveforms of over 2151 teleseismic events ($M_w > 5.8$)
28 from 2009 to 2021, recorded at permanent and temporary stations in and
29 around Mongolia. The multi-mode dispersion curves of Love and Rayleigh
30 waves were extracted using the nonlinear waveform fitting method for in-
31 dividual seismograms. Then, we retrieved phase speed maps for each mode
32 and frequency, incorporating finite-frequency effects. Finally, localized multi-
33 mode dispersion curves extracted from the phase speed maps were inverted
34 for local anisotropic 1-D S-wave profiles, forming a 3-D shear wave model.
35 Our new model exhibits significant lateral variations of S wave speeds at
36 70–100 km depth beneath Mongolia, i.e., slow anomalies in the tectonically
37 active western Mongolia and fast anomalies in stable eastern Mongolia. In

the radial anisotropy model, SH waves are faster than SV waves in almost the entire Mongolian lithosphere above 100 km depth, except for the northern Altay Mountains region. The Hangay Dome region is characterized by significantly slower velocities, indicating the asthenospheric upwelling that causes the uplifting of this region. This study reveals distinct lateral variations of S wave speeds across the boundary between the Amurian and Eurasian plates, characterized by the prominent fast anomaly of the dipping lithosphere at the western edge of the Amurian plate.

Keywords: surface wave, tomography, upper mantle, lithosphere, Mongolia, Amurian plate

1. Introduction

Mongolia is located inside the East Asian continent, bounded by the Siberian craton in the north, and affected by the India-Asia collision zone in the south and by the far-field subduction zone of the Pacific plate in the east (Figure 1). The Central Asian Orogenic Belt (CAOB), a long-lasting accretionary orogen that spans much of central and eastern Asia, includes Mongolia. The CAOB, extending from North China Cratons and the northern margins of Tarim to the northern Baikal Rift region, is one of the biggest Paleozoic orogens from the Mesoproterozoic to Paleozoic, with the accretion of ophiolites, oceanic islands, accretionary wedges, island arcs, and microcontinental fragments (Windley et al., 2007). Due to the collision of the Indian and Eurasian plates as well as the subduction of the Pacific and Philippine Sea plates beneath Japan, East Asia has experienced extensive tectonic deformations during the Cenozoic (Wei et al., 2012). India has been moving

steadily northward since 55 million years ago, raised the Himalayas and Tibetan Plateau, and controls tectonics in western China and Mongolia (Molnar and Tapponnier, 1975; Hao et al., 2019). Nonetheless, the subductions of the Pacific and Philippine Sea plates have been significant contributors to the tectonic stress in Asia, producing island arcs, marginal seas, and continental rifting (Huang and Zhao, 2006; Hao et al., 2019). The creation of continental rifts and active intraplate volcanoes in Northeast China is also suggested by tomographic images to be related to the dynamic processes of the Western Pacific and East Asia because the subducted Pacific plate stagnates in the mantle transition zone beneath East China (Huang and Zhao, 2006). There are several intra-plate volcanoes in Mongolia, Korean Peninsula, and China (Global Volcanism Program, 2023). Figure 1 displays the locations of Taryatu Chulutu (TC), Khanuy Gol (KG), Bus Obo (BO), Middle Gobi (MG), and Dariganga (DG) volcanic eruption sites from the Late Cenozoic. According to Hunt et al. (2012), Mongolia’s volcanism comprises several alkali-basalt cones that have been erupting for about 30 million years. Even though the greatest lava flows occur in the eastern Dariganga, the majority of modern volcanism is located near the Hangay Dome and the south of the Baikal Rift.

The Amurian plate is in northeastern Asia, covering northeast China, the Korean Peninsula, the Sea of Japan, the eastern shore of Lake Baikal in southeast Russia, and eastern Mongolia. The Amurian plate was postulated as a distinct plate from the Eurasian plate that is moving toward the southeast. The border between these two plates is thought to be confirmed by the Baikal Rift Zone (Zonenshain and Savostin, 1981). Western Mongolia belongs to the Eurasian plate, whereas Eastern Mongolia belongs to the

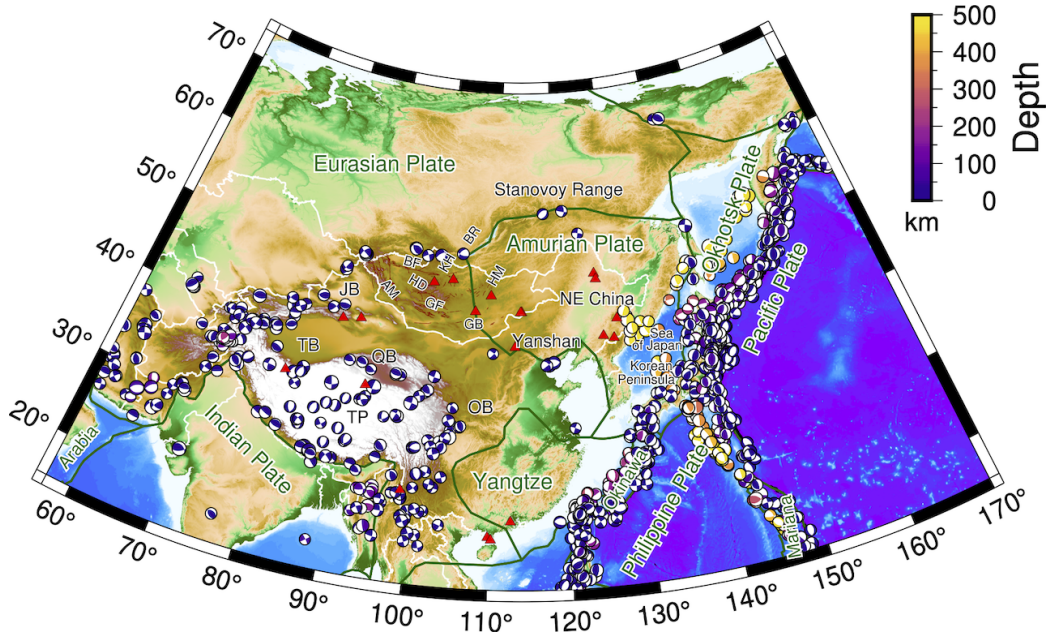


Figure 1: Dark green lines indicate plate boundaries. Triangles represent Holocene volcanoes (Global Volcanism Program, 2023). Focal mechanisms greater than Mw 6.0 from the Global CMT catalog between 1976 and 2022 (Ekström et al., 2012). Abbreviations from west to east: TB = Tarim Basin, JB = Junggar Basin, TP = Tibet Plateau, QB = Qaidam Basin, AM = Altay Mountains, BF=Bulnay Fault, HD = Hangay Dome, GF=Gobi Altay Fault, KH = Khovsgol, BR = Baikal Rift, GB = Gobi Basin, HM = Hentey Mountains, OB = Ordos Basin.

87 Amurian plate. The N-S compression by the convergence of the Indian plate
 88 and Tibetan Plateau affects western Mongolia, while the back-arc extension
 89 by the subduction of the Pacific plate influenced E-W oriented tectonics in
 90 eastern Mongolia (Meng et al., 2003).

91 GPS measurements in western Mongolia showed that northward shorten-
 92 ing decreases from south (10 mm/year) to north (4 mm/year) in the Altay
 93 region, but central and eastern Mongolia moves eastward/southeastward mo-

94 tion at 4mm/year (Calais et al., 2003). This transition area dominates the
 95 Hangay Dome region, characterized by a high topography, comparatively flat
 96 plateau, and widespread Quaternary basalts. The Hangay topography is of-
 97 ten regarded as a relatively recent formation that was elevated and formed
 98 within the past 20 – 30 million years (Walker et al., 2007), and the greatest
 99 active stage from 3 – 4 Ma until now (Barry and Kent, 1998). However, Mc-
 100 Dannell et al. (2018) indicated that this mountain environment is very old
 101 and has endured for almost 100 million years based on the geochemical and
 102 geological evidence. From geochemical and petrological investigations, Erde-
 103 nesaihan et al. (2013) discussed the tectonic formation history of the Hangay
 104 region, which is considered an accretionary orogen formed through the clo-
 105 sure of the Hangay-Hentey paleo-ocean during the early Paleozoic through
 106 early Mesozoic. Two seismically active strike-slip faults, the Bulnay Fault
 107 and the Gobi-Altay Fault, which generated gigantic ($M \geq 8.0$) intraconti-
 108 nental earthquakes, are situated respectively north and south of the Hangay
 109 Dome (Walker et al., 2007). Distant influences of the India-Asia convergence,
 110 Pacific plate subduction, mantle plume activity, convective mantle flow, and
 111 magmatic underplating have all been implicated in the mountainous terrain
 112 of the Mongolian plateau (Molnar and Tapponnier, 1975; Windley and Allen,
 113 1993; Cunningham, 2001; Petit et al., 2002; Zorin et al., 2006; Petit et al.,
 114 2008). Thus, the Hangay Dome is one of Mongolia’s most complex and enig-
 115 matic tectonic features that remains debated.

116 Previous geophysical studies present controversial models which can be
 117 categorized into two major hypotheses. One supposes high topography and
 118 intraplate volcanism are formed due to the deep-rooted mantle plume (Wind-

119 ley and Allen, 1993; Zorin et al., 2006). The regional heat flow measurements
 120 with 60–70 mW/m² in the Hentey Mountains and Hangay Dome (Khutorskoy
 121 and Yarmoluk, 1989), lithospheric thinning (Zorin et al., 1990), and late
 122 Cenozoic alkaline volcanism (Hunt et al., 2012) supported the mantle plume
 123 hypothesis. Also, Chen et al. (2015a) suggested a low-velocity zone could be
 124 caused by hot fertilized peridotite detached from the stagnant Pacific slab
 125 as it falls to the lower mantle (Zorin et al., 2006) from a large tomographic
 126 image in East Asia. Another hypothetical model is a lithospheric model,
 127 which can be explained as the dispersed locations of the potential melting
 128 zones (Cunningham, 2001; Barry et al., 2003). This scenario is consistent
 129 with a strong negative gravity model (Petit et al., 2002), the result of mag-
 130 netotelluric inversions (Comeau et al., 2018), thermo-mechanical numerical
 131 modeling (Comeau et al., 2021), and recent tomography models (Feng, 2021;
 132 Wu et al., 2021; Wang et al., 2022).

133 Mongolia and the neighboring regions have been investigated using var-
 134 ious seismic tomography as a part of the wider regional models covering
 135 eastern and central Asia (e.g., Tiberi et al., 2008; Chen et al., 2015b,a; He
 136 et al., 2016; Tao et al., 2018; Wu et al., 2021; Zhao et al., 2021; Witek et al.,
 137 2021; Feng, 2021; Huang and Zhao, 2022; Wang et al., 2022; Li et al., 2022).
 138 Recent local-scale investigations in western and central Mongolia, especially
 139 in Hangay Dome, indicated a thinner lithosphere (60–80 km) contrasted to
 140 the surrounding areas, while the crust was found to be as thick as about
 141 50–55 km (Petit et al., 2008; Feng, 2021; Zhao et al., 2021). Low-velocity
 142 anomalies were seen in the upper mantle at around 70–150 km depths (Tiberi
 143 et al., 2008; Chen et al., 2015a; Comeau et al., 2018; Wu et al., 2021; Feng,

2021; Wang et al., 2022; Huang and Zhao, 2022).

In contrast to western Mongolia, eastern Mongolia has been less investigated, mainly due to poor seismic station coverage. A receiver function result of He et al. (2016) showed the crustal thickness varies between 38 and 46 km, and Rayleigh-wave phase speed maps by Yu et al. (2015); Pan et al. (2015) exhibited high-velocity anomalies in Southern Gobi and Hangay-Hentey basin while low-velocity anomalies in Middle Gobi. Using traveltimes tomography, Zhang et al. (2017) found slow P and S velocities under the Hentey Mountains and areas close to the comparatively low-lying Gobi Desert. Rayleigh-wave tomography by Wang et al. (2022) suggested that consistently faster upper mantle velocities may indicate the strong lithosphere beneath the East Gobi Desert.

Although various seismological studies have been done in and near Mongolia, nationwide regional seismological images beneath the whole areas of Mongolia with uniform station coverage using seismic surface waves have not yet been obtained. Thus, the detailed 3-D structure of the entire Mongolian upper mantle, including radial anisotropy, remains still largely unknown. The aim of this study is to construct a new 3-D upper-mantle S-wave speed model including radial anisotropy beneath central Eurasia around Mongolia with multimode surface waves using many permanent and temporary broadband seismic stations inside Mongolia. Such a high-resolution 3-D model will enable us to clarify the relationship between the current Mongolian tectonics and mantle dynamics. In this study, we employ the three-stage inversion technique by Yoshizawa and Kennett (2004); Yoshizawa (2014). The 3-D distributions of SV and SH wave speeds are obtained from dispersion data

169 of multimode Love and Rayleigh waves recorded at the permanent and tem-
170 porary Mongolian networks and neighboring GSN, PASSCAL, and NECES-
171 SArray networks. The new 3-D model provides a high-resolution image of
172 lateral structural variations between the Eurasian and Amurian plates, indi-
173 cating new seismological evidence of an enigmatic boundary at the western
174 border of the Amurian plate.

175 **2. Data and method of multimode phase speed measurements**

176 *2.1. Seismic stations and events*

177 We employed three-component broadband seismograms of the permanent
178 and temporary Mongolian networks, Global Seismograph Network (GSN),
179 Central Mongolian Seismic Experiments (Meltzer et al., 2019) (PASSCAL
180 network), and temporary networks in Northeast China (NECESSArray). In
181 total, 455 broadband seismic stations (Figure 2) are used. We have analyzed
182 2151 teleseismic events with a moment magnitude 5.8 or higher, located at
183 an epicentral distance longer than 1000 km (Figure 3). At first, all original
184 waveforms are deconvolved with corresponding instrument responses. Then,
185 the horizontal components are rotated to the radial and transverse compo-
186 nents. Using the vertical and transverse components independently, a large
187 number of path-average multimode phase speeds of Rayleigh and Love waves
188 are measured for each event-station path across the target area using the
189 single-station waveform fitting method, as described in the next section.

190 *2.2. Multimode phase speed measurements*

191 As the initial step for the three-stage inversion of surface wave tomog-
192 raphy (Kennett and Yoshizawa, 2002; Yoshizawa and Kennett, 2004), we

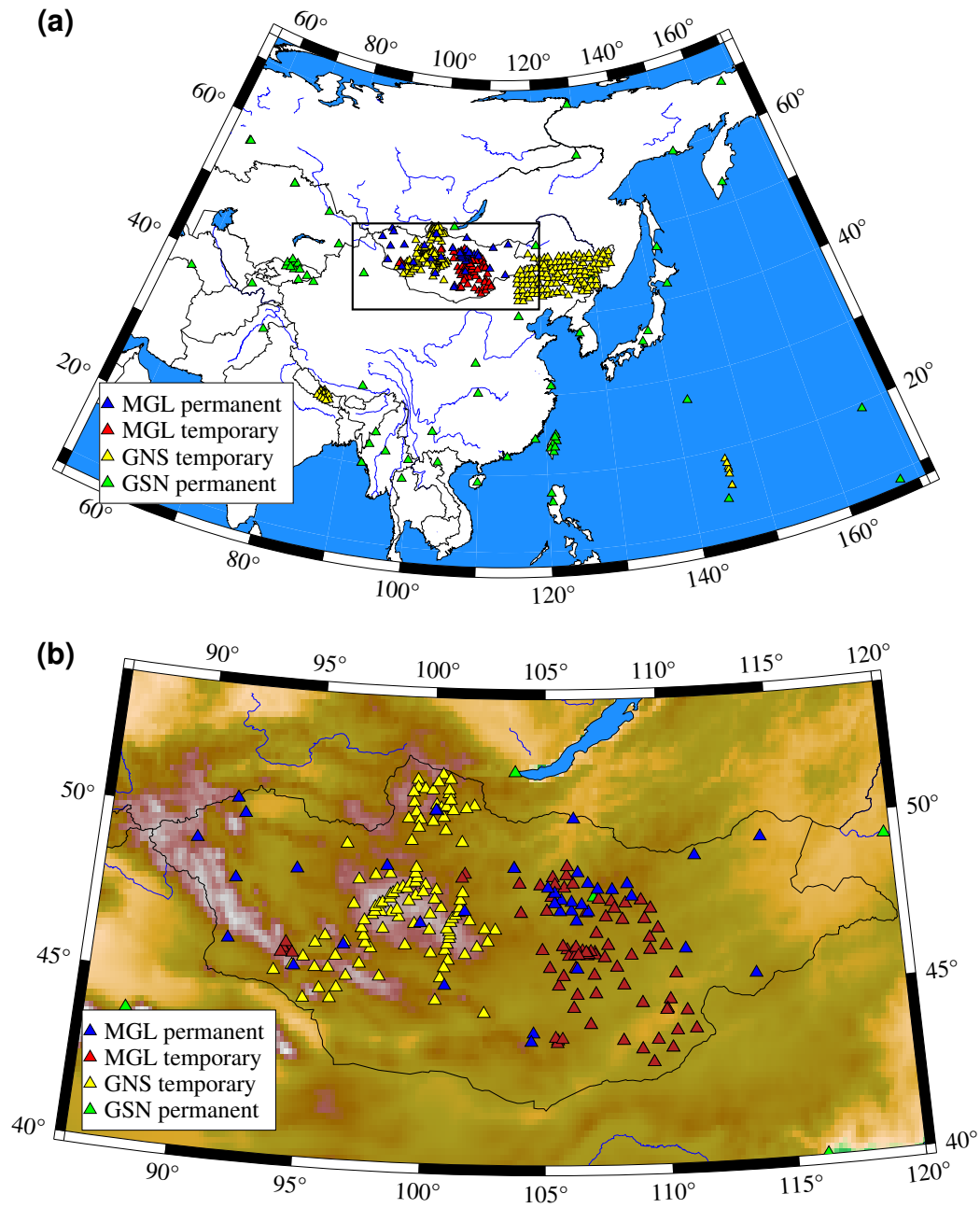


Figure 2: Seismic stations used in this study. a) All stations, b) stations in Mongolia.

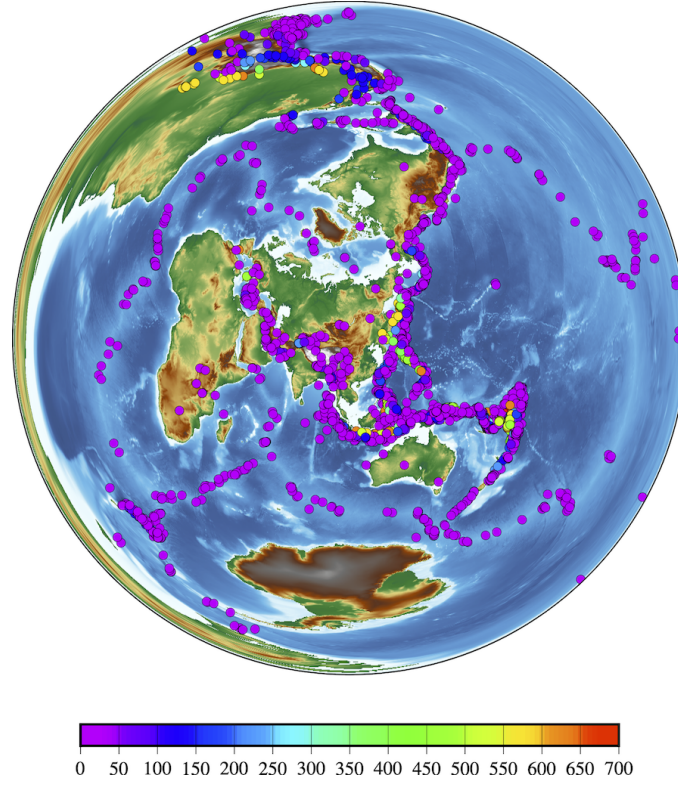


Figure 3: Employed seismic events with a moment magnitude greater than 5.8 from 2009 to 2021.

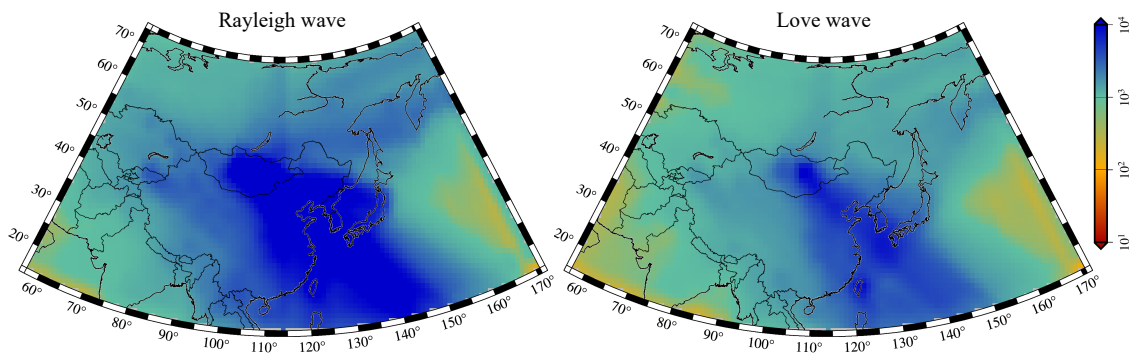


Figure 4: Ray-path density of the fundamental-mode Rayleigh and Love wave at 100 s. Ray paths count in 2x2 (degree) grids.

193 performed fully nonlinear waveform inversion for path-specific 1-D S-wave
 194 profiles by fitting observed and synthetic waveforms based on global opti-
 195 mization (Yoshizawa and Kennett, 2002b; Yoshizawa and Ekström, 2010).
 196 The details of the automated measurement procedure have been explained
 197 by Yoshizawa and Ekström (2010). Here we summarize the essence of the
 198 measurement technique briefly.

199 For each event-station path, more than 5000 path-specific 1-D S wave pro-
 200 files are sampled using the Neighborhood Algorithms by Sambridge (1999),
 201 which is used as a global optimizer. The surface-wave WKBJ method is used
 202 to compute synthetic waveforms for all models by employing the focal mech-
 203 anism from the global CMT catalog (Ekström et al., 2012). Multiple time
 204 windows are selected automatically for the fundamental and higher modes
 205 based on the predefined group-speed ranges. Waveform misfits between the
 206 synthetic and observed seismograms are assessed in these time windows with
 207 multiple bandpass filters from 5 to 30 mHz for the fundamental mode and
 208 up to 50 mHz for the higher modes. Then, the best 1-D profile, which pro-
 209 vides the minimum waveform misfit, is selected and used to compute the
 210 path-average multimode phase speeds for each path. To evaluate the qual-
 211 ity of measured phase speeds, we employ the frequency-dependent reliabil-
 212 ity parameter computed from the relative power of each mode and relative
 213 waveform fit as defined by Yoshizawa and Ekström (2010). In this study,
 214 we employed the same *a priori* constraints and thresholds as Yoshizawa and
 215 Ekström (2010) for selecting reliable dispersion measurements and outlier
 216 removal.

217 Our dataset consists of about 87,000 paths for the fundamental-mode

218 Rayleigh waves, about 50,000 paths for the fundamental-mode Love waves
 219 at a period of 100 s, and about 20,000–50,000 paths for higher modes of both
 220 Rayleigh and Love waves (Figure S1). An example of the ray path coverage
 221 for the fundamental-mode Rayleigh and Love waves at 100 s is displayed in
 222 Figure 4. The entire study region is covered well with the dense ray paths
 223 owing to many broadband seismic stations deployed there. We could obtain
 224 high ray-path density with good azimuthal coverage in East Asia and Mon-
 225 golia. As described in the subsequent section, we reconstructed phase speed
 226 maps for each mode and frequency, for which we could gather more than 5000
 227 paths. These multi-mode phase speed maps are employed to compute a 3-D
 228 shear wave model of the continental lithosphere and asthenosphere beneath
 229 central Eurasia around Mongolia.

230 **3. Multimode phase speed mapping**

231 The measured multimode phase speeds in the first step are used to retrieve
 232 phase speed maps in the second step. We used linearized tomographic inver-
 233 sion incorporating approximate effects of finite-frequency for surface waves
 234 around the great-circle paths (Yoshizawa and Kennett, 2002a). The proce-
 235 dure of phase speed mapping has been explained by Yoshizawa and Kennett
 236 (2004) and Yoshizawa (2014) in detail. Phase speed distribution is expanded
 237 in spherical B-spline functions at rectangular grids. The grid spacing of this
 238 study depends on the ray path coverage for each mode and frequency; i.e.,
 239 2.0° for the fundamental mode with more than 30,000 paths, 3.0° for more
 240 than 15,000 paths, 4.0° for more than 8,000 paths, and 5.0° for all modes
 241 with more than 5000 paths.

242 *3.1. Resolution test*

243 We performed checkerboard tests to clarify the lateral resolution of our
 244 tomography model. The input checkerboard models contain velocity fluctua-
 245 tions of around $\pm 5\%$ from the reference velocity at each frequency. Various
 246 cell sizes are tested to examine the spatial resolution of phase speed models.
 247 Figure 5 displays examples of the resolution tests for the fundamental-mode
 248 Rayleigh and Love wave at 100 s with $3.0^\circ \times 3.0^\circ$.

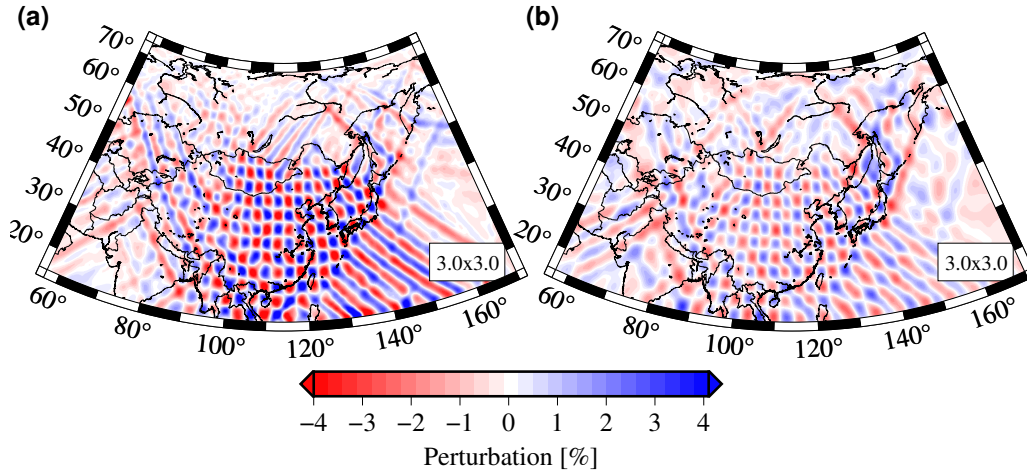


Figure 5: Outputs of checkerboard tests for the fundamental-mode Rayleigh and Love waves at 100 s with 3.0° cells.

249 We also show additional checkerboard tests for the fundamental- and sec-
 250 ond higher-mode Rayleigh and Love waves at 100 seconds in Figure S3 and
 251 Figure S4, respectively (in Supporting Information). The retrieved checker-
 252 board patterns in Figure S3 suggest that our data set achieves acceptable
 253 lateral resolution with cell sizes of $2.0^\circ \times 2.0^\circ$ or greater for Rayleigh-wave
 254 maps beneath Mongolia owing to many crossing paths with various direc-

255 tions in each cell. The checkerboard results indicate that the southern and
 256 central parts of the study regions are particularly well resolved by denser ray
 257 coverage. In contrast, the rest parts show somewhat smeared patterns due
 258 to limited numbers of crossing paths. With smaller numbers of available ray
 259 paths, the lateral resolution of higher-mode Love waves tends to be limited
 260 compared to that of Rayleigh waves, although the large-scale features greater
 261 than $3\text{--}4^\circ$ can be mostly recovered.

262 *3.2. Multimode phase speed maps*

263 The phase speed maps are acquired in the 30–200 s period range for
 264 Rayleigh, and 33–200 s for Love waves, depending on modes. The period
 265 ranges for all modes are summarized in Table S1 (Supplementary Informa-
 266 tion). We performed jackknife resampling tests to estimate standard errors
 267 in our multimode phase speed maps. The results of the jackknife resampling
 268 tests for phase speed maps are displayed in Figure S5 (section S3 in Support-
 269 ing Information). The estimated errors for the fundamental-mode Rayleigh
 270 wave at 100 s with an average phase speed of 4.13 km/s are mostly less
 271 than 0.052 km/s, while those for the second higher mode Love wave at 100
 272 s with an average phase speed of 7.37 km/s are around 0.11 km/s. Figure 6
 273 shows examples of phase speed maps for the fundamental- and higher-modes
 274 of Rayleigh and Love waves. Additional multimode phase speed maps for
 275 Rayleigh and Love waves are summarized in Figures S6-S9 (section 4 in Sup-
 276 porting Information). The average phase speed C_0 shown in each map is used
 277 as a reference for the representation of fractional phase speed perturbations.
 278 The reference phase speed is derived from the average in the whole area of
 279 this study. The large-scale features of the fundamental-mode maps show

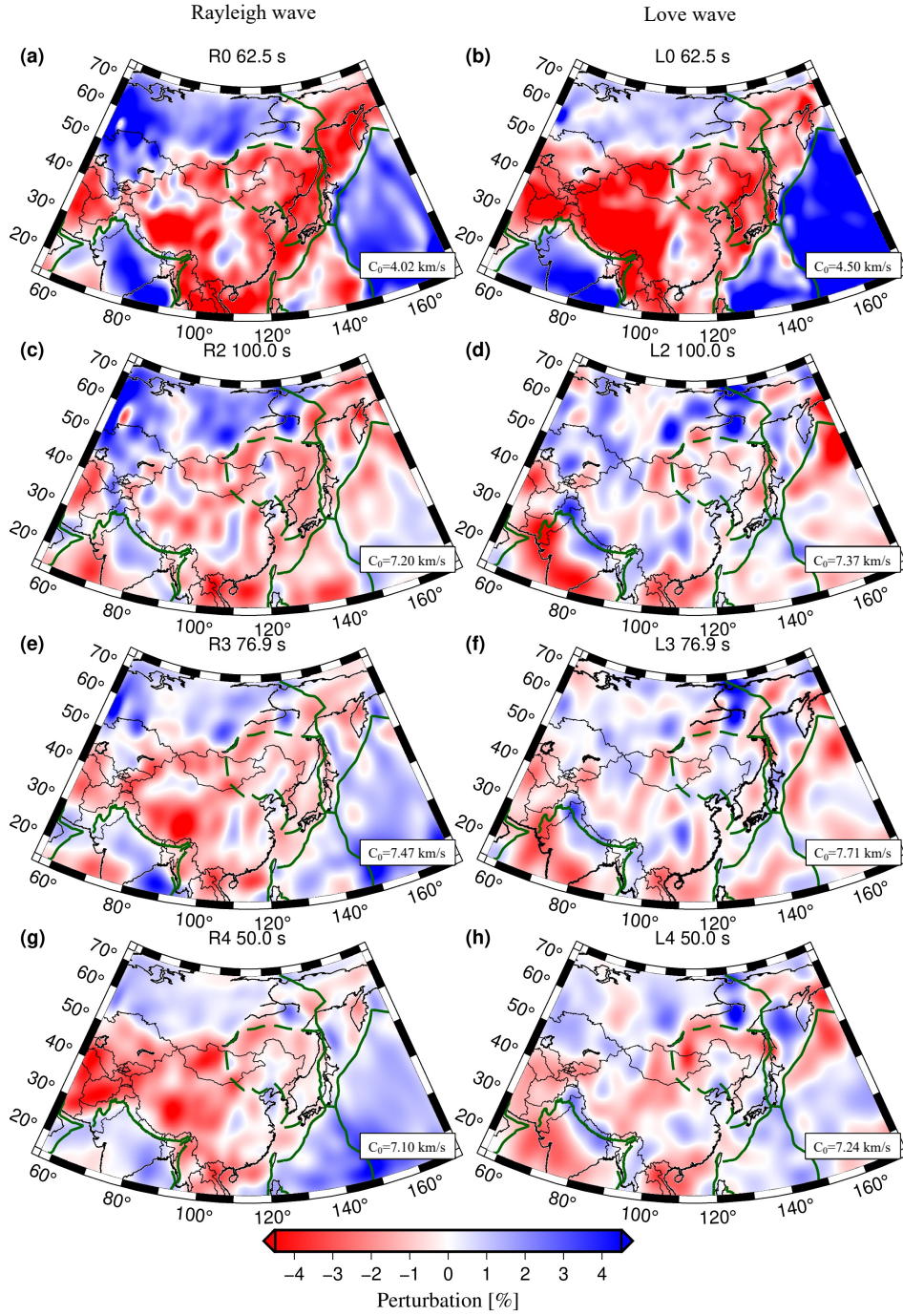


Figure 6: Phase speed maps for the fundamental- and higher-modes of the Love (L) and Rayleigh (R) waves, and the numbers indicated are mode number and period.

fast anomalies in the Siberian craton, Tarim basin, and Ordos area and slow anomalies in Tibet, Okhotsk, and western Mongolia. The overall patterns of the phase speed distribution of Rayleigh and Love waves are consistent with the global model GDM52 (Ekström, 2011). Still, our lateral resolution in this region is much higher than the global model.

4. Radially anisotropic 3-D S wave model

4.1. Inversions for radially anisotropic 1-D S wave models

Following Yoshizawa (2014), we used the generalized nonlinear least-squares inverse scheme of Tarantola and Valette (1982) to build the 3-D radially anisotropic S-wave model using the multimode phase speed maps. The detailed procedure has been described by Yoshizawa (2014). Here we consider a set of 6 independent model parameters (ρ , α_H , α_V , β_H , β_V , η), where ρ is density, α_H and α_V represent horizontally and vertically polarized P wave speeds, β_H and β_V represent horizontally and vertically polarized S wave speeds, η is a dimensionless anisotropic parameter. P wave speeds and density are considered via scaling relations for S wave speeds (e.g., Gung et al., 2003; Panning and Romanowicz, 2006) following (Montagner and Anderson, 1989). To control the amplitude of shear wave perturbations and the smoothness of the velocity model during the inversions, we employ the model covariance matrix comprising two *a priori* parameters, standard deviations σ and correlation length L (Yoshizawa and Kennett, 2004; Yoshizawa, 2014). We used the following *a priori* values, i.e., $\sigma = 0.045$ km/s and $L = 10$ km in the depth range between Moho and 400 km, and $L = 15$ km between 400 and 670 km. Beneath 670 km depth, σ decreases linearly to 0.025 km/s,

while L increases linearly to 30 km at 1500 km depth. The crustal velocity can be perturbed with $\sigma = 0.025$ km/s and $L = 5$ km. Thus, the crust and uppermost mantle structures change rapidly while the deeper structure changes gradually.

We performed a series of tests to examine the effects of the crustal corrections on the shear wave speed model using two reference crustal models and without the crustal correction. Figure S10 (section 5 of Supporting Information) shows the comparisons of the retrieved shear wave models with crustal corrections with 3SMAC (Nataf and Ricard, 1996) and CRUST1.0 (Laske et al., 2013), and without the crustal correction using a modified PREM (Dziewonski and Anderson, 1981) with a smoothed 220 km discontinuity. Below 150 km, the crustal correction has little impact on the deeper part of the shear wave model, although there are some variations above 150 km. In this study, we employed the local reference models combining the modified PREM (smoothed 220 km discontinuity) and the CRUST1.0 model because the crustal thickness of the CRUST1.0 model is more suited, particularly in western Mongolia. We also performed the vertical resolution tests summarized in Figure S11 (section 5 in Supporting Information), which indicate sufficient vertical resolution down to 300 km depth, despite the vertical smearing due to the long-period surface waves.

4.2. 3-D model in central Eurasia and Mongolian regions

Based on the retrieved SH (β_H) and SV (β_V) models, we consider their Voigt average as the isotropic S wave model, $\beta_{iso} = \sqrt{(2/3)\beta_V^2 + (1/3)\beta_H^2}$ (e.g., Panning and Romanowicz, 2006) and the radial anisotropy parameter $\xi = (\beta_H/\beta_V)^2$. Figure 7 (a-d) shows the final 3-D isotropic S wave and radial

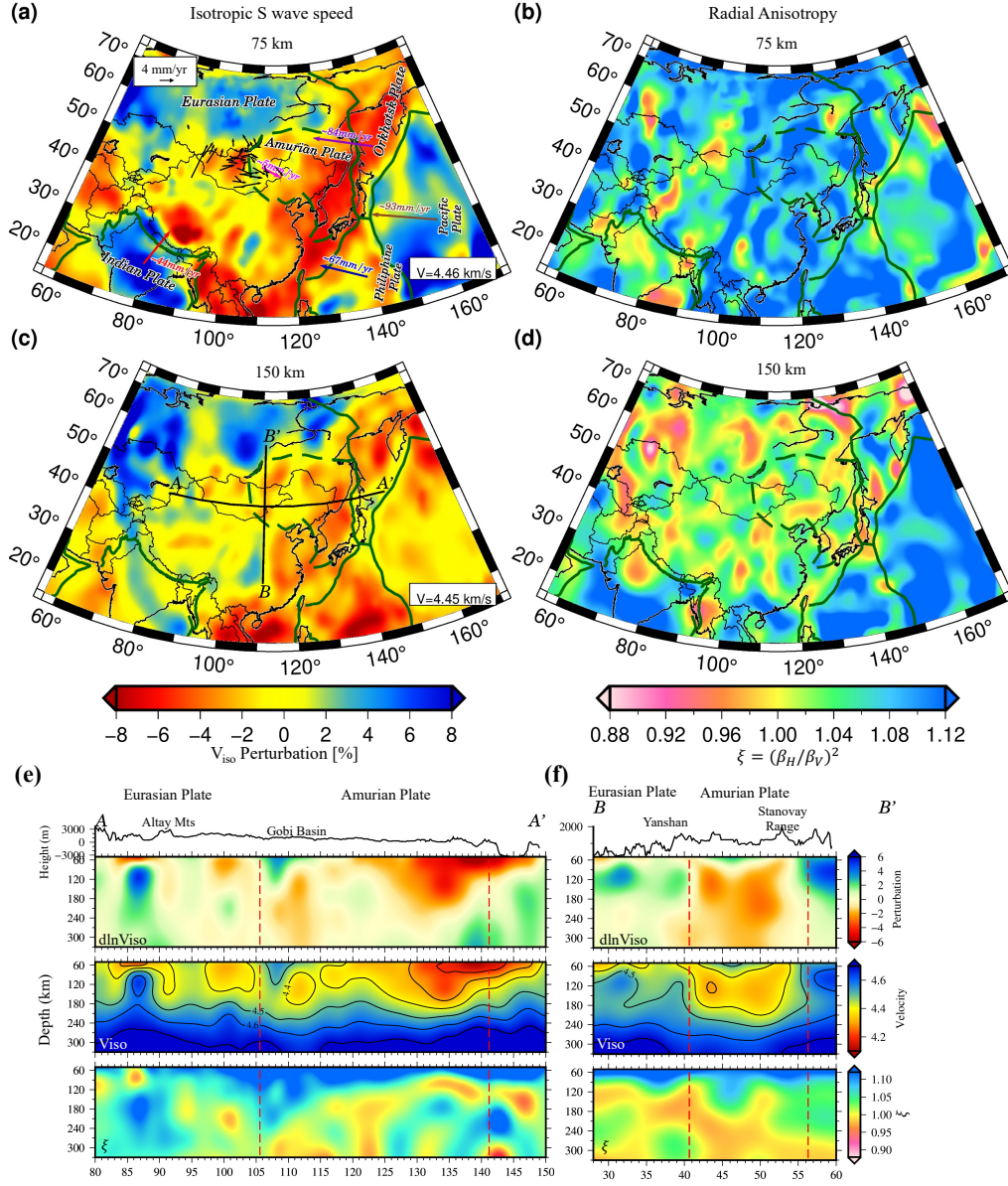


Figure 7: (a, c) 3-D isotropic S wave speed model at 75 and 150 km depths calculated as the Voigt average of retrieved SH and SV wave speeds, and (b, d) corresponding radial anisotropy parameter $\xi = (\beta_H/\beta_V)^2$. Plate boundaries (green solid lines) are taken from Bird (2003). (a) Black arrows in and around Mongolia denote the rates of crustal motion relative to Eurasia (Calais et al., 2003). The other colored arrows indicate relative plate motions based on the MORVEL plate model (DeMets et al., 2010). (e, f) Cross-sections of isotropic S wave speed perturbation (top), absolute isotropic S wave speed (middle), and radial anisotropy parameter (bottom) along the profiles A-A' and B-B' with surface topography on top. The major tectonic provinces are labeled on topography. The vertical red dashed lines show the vertical extension of the Amurian plate boundary at the surface by Bird (2003).

329 anisotropy models in the whole region of this study. The regionally-averaged
330 1-D profiles in Figure S12 ((a) Eurasian and (b) Mongolian regions) are used
331 as local reference models for the isotropic S wave speed perturbations of our
332 tomography models, while radial anisotropy is displayed as a deviation from
333 isotropy ($\xi = 1$). The average 1-D profiles of the SV and SH wave speeds
334 in the broader Eurasian region are similar to the anisotropic PREM model
335 (Figure S12(a)), but those in the Mongolian region tend to exhibit slower
336 shear wave speeds (Figure S12(b)). In the upper 180 km, the average radial
337 anisotropy in Mongolia is a few percent lower than that of PREM, reflecting
338 local tectonic features under Mongolia.

339 For the 3-D model plots in this study, we have applied the Gaussian
340 filter with a standard deviation of 0.67° to smooth our 3-D velocity model
341 laterally. In our model at 70–100 km depth, we find relatively low velocities
342 in western Mongolia, Tibet, and in the East and South China Seas, Yellow
343 Sea, Ryukyu Trench, Sea of Japan, and Sea of Okhotsk, while other areas
344 in the Siberian craton, Sichuan basin (Yangtze cratons), Ordos block, Tarim
345 basin, and eastern Mongolia exhibit higher velocities. At a depth of 150
346 km, the low-velocity anomalies in western Mongolia and Tibet are vanished,
347 while the eastern marginal seas still show slower anomalies. The fast S-wave
348 anomalies in the Tarim, Yangtze, and Sichuan basins are apparent in the
349 isotropic S wave model down to 150 km depth. Earlier surface wave studies
350 agree with the overall pattern of shear wave speed anomalies in the upper
351 mantle (Ritzwoller et al., 2002; Chen et al., 2015b; Tao et al., 2018; Witek
352 et al., 2021).

353 SH and SV wave speeds and radial anisotropy models are shown at various

depth slices in Figure S13 (section 5 in Supporting Information). In the radial anisotropy maps at 70–120 km depth, most regions exhibit positive radial anisotropy ($\xi > 1$ or $V_{SH} > V_{SV}$), except for a part of Tibet, northwest Mongolia, and under Japan. At the same depth range, radial anisotropy with very slow SV wave speeds can also be found in Tibet, western Mongolia (Hangay Dome), and eastern subduction regions. Below 150 km depth, the strength of radial anisotropy tends to be weaker than shallower depth in most of the region. Figures S14 to S16 (Supporting Information) summarize vertical cross-sections (E-W and N-S directions) of SH and SV wave speeds and radial anisotropy at various locations. In the following section, we will focus our discussion on the characteristic seismic structure in the Mongolian region.

5. Discussion of Mongolian Upper Mantle Structure

The lateral structural changes revealed by our new 3-D S-wave model beneath the Mongolian region suggest some intriguing geographical relations that reflect Mongolian tectonics and mantle dynamics. Here we focus on the S-wave structure in the upper mantle from 60 to 300 km depth, which has been well resolved by our surface wave dispersion data.

5.1. Entire Mongolia

Figure 8 (a-d) displays the isotropic S wave speed and radial anisotropy models at 70 and 120 km depths in the Mongolian region. Figure S17 (Supporting Information) displays various depth slices of the original SH and SV wave speed models and the radial anisotropy ξ beneath Mongolia. Figures

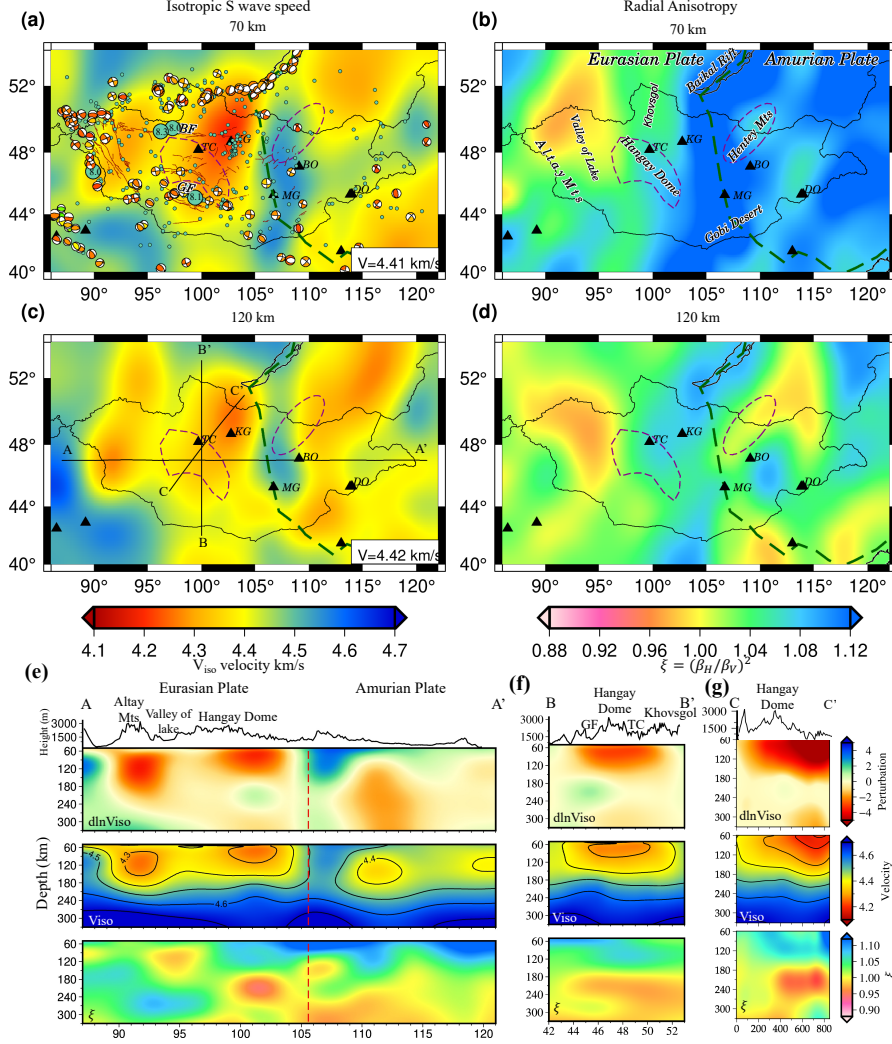


Figure 8: Isotropic S wave speed model and radial anisotropy parameter $\xi = (\beta_H/\beta_V)^2$ at 70 and 120 km depths beneath the Mongolian region. The black triangles denote the Holocene volcanoes; Taryatu Chulutu (TC), Khanuy Gol (KG), Middle Gobi (MG), Bus Obo (BO), and Dariganga (DG). (a) Isotropic S wave speed at 70 km depth with seismicity in and around Mongolia. Green circles indicate seismic events from the catalog by IAG (Institute of Astronomy and Geophysics of Mongolia) (Jan 1964- May 2023, $M_I \geq 3.5$); Some historical large earthquakes ($M_w \geq 8.0$) are labeled. Focal mechanisms greater than $M_w 4.0$ are taken from the Global CMT catalog between January 1976 and May 2023 (Ekström et al., 2012). Green dashed lines are the expected Amurian plate boundary by Bird (2003). (e, f, g) Cross-sections of isotropic S-wave speed perturbation, absolute isotropic S-wave speed, and radial anisotropy along profiles A-A', B-B', and C-C' with surface topography on top. Main tectonic domains are labeled on topography. A vertical red dashed line in the cross-section indicates the vertical extension of the boundary between the Eurasian and Amurian plates from Bird (2003).

377 S18–S20 summarize the corresponding vertical cross-sections. Figure S21 dis-
 378 plays the 3-D views of (a, b) slow and fast shear wave speed anomalies and (c,
 379 d) radial anisotropy beneath the Mongolian region. In the shallower depth
 380 at 70–100 km beneath Mongolia, the S-wave speeds are generally slower in
 381 the tectonically active western area and become faster in the relatively stable
 382 eastern area. Slower velocities in western and central Mongolia are also seen
 383 in earlier tomography models (e.g., Ritzwoller et al., 2002; Chen et al., 2015a;
 384 Tao et al., 2018; Witek et al., 2021; Li et al., 2022).

385 In western Mongolia, some distinctive slow velocity anomalies are seen
 386 in the southeastern area of the Khovsgol rift zone, eastern Hangay dome,
 387 Mongol Altay, and Valley of the Lake. On the contrary, in the eastern re-
 388 gions at shallower depths from 70 to 100 km, the fast anomalies are observed
 389 in Southern Gobi, Hentey Mountains, and Middle Gobi. The high-velocity
 390 anomaly in Middle Gobi is still prominent even at a greater depth of around
 391 170 km, while that in the Hentey Mountains and South Gobi has essentially
 392 disappeared by that depth. This high-velocity anomaly may indicate dip-
 393 ping or delaminated lithosphere, which can be affected by small-scale mantle
 394 convection, which may affect the east-to-west movement of eastern Mongo-
 395 lia. From the plate boundary model by Bird (2003), the Eurasian-Amurian
 396 plate border coincides well with the location where the lithosphere of east-
 397 ern Mongolia dips westward, particularly in the region between the latitudes
 398 44°N and 50°N, and between the longitudes 105°E and 110°E. We also note
 399 that a clear velocity contrast between western and eastern Mongolia extends
 400 down to 250 km depth (Figure 8 (e)), which may indicate the vertical exten-
 401 sion of the Eurasian and Amurian boundary, as we will discuss in detail in

402 Section 5.3.

403 The radial anisotropy model exhibits a faster SH wave speed than SV in
404 nearly the entire Mongolian lithosphere above 100 km depth, except for the
405 northern part of the Altay Mountains, where both SH and SV wave speeds
406 are slower than average with anomalous radial anisotropy with $SV > SH$ (Fig-
407 ure S17), especially at depths of about 75–130 km. The Altay and Sayan
408 Mountains have experienced strong convergence as a result of the northward
409 motion of the Asian blocks (such as Junggar and Tarim Basins) due to the
410 India-Asia collision (Huang and Zhao, 2022). The P-wave velocity model
411 by Huang and Zhao (2022) showed low velocity down to 200 km depth be-
412 neath the Altay Mountains, suggesting that lithosphere-scale interactions
413 may cause it. Our S-wave model also shows the low-velocity anomalies along
414 the northern Altay Mountain border, which can persist to about 300 km
415 depth (Figure S19).

416 The Hentey Mountains also show slower SH wave speed anomaly at depths
417 between 100 and 200 km. The notable low velocity found under the Hentey
418 Mountains agrees well with a recent tomographic study by Chen et al. (2015a)
419 who have reported the low-velocity anomaly may stretch from the uppermost
420 mantle to 200 km depth at least. He et al. (2019) noted that the tectonic
421 setting and dynamic processes beneath the Hentey Mountains and Hangay
422 Dome are distinctive. They also suggested that low-velocity anomalies be-
423 neath the Hentey Mountains could indicate partially molten or heated ma-
424 terial in the upper mantle. Our radial anisotropy model suggests that the
425 low-velocity anomalies with radial anisotropy of $SV > SH$ beneath the Hentey
426 Mountains might reflect mantle upwelling (Figure S19 (a and b) and Figure

427 S20 (i1)).

428 Figure 9 illustrates the schematic west-east cross section across Mongolia
429 based on our tomography model, indicating the major structural features and
430 lateral variations in the upper mantle beneath western and eastern Mongo-
431 lia. Typical three-dimensional views of our model with isocontour plots are
432 displayed in Figure S21 in Supplementary Information. In the subsequent
433 sections, we will further discuss the major features illustrated in Figures 9
434 and S21, such as the uplifting Hangay Dome region with mantle upwelling
435 in western Mongolia (Eurasian plate), and relatively thick and dipping litho-
436 sphere, which may reflect a plausible lithospheric drip or delamination in
437 eastern Mongolia (Amurian plate). The significant structural variations be-
438 tween western and eastern Mongolia can be related to the differential plate
439 motion between the Eurasian and Amurian plates.

440 5.2. Western Mongolia: Hangay region

441 The Hangay Dome in western Mongolia is considered one of the most
442 significant tectonic units in this region. Significant earthquakes have not been
443 recorded in the Hangay Dome itself, but some major earthquakes occurred
444 around this area, e.g., the Mw 7.1 earthquake (1967) on the Mogod fault to
445 the east of the Hangay Dome, Mw 8.3 earthquake (1905) on the Bolnay fault
446 to the north, and Mw 8.1 Gobi-Altay earthquake (1957) on the Bogd faults
447 to the south. As mentioned earlier, existing seismic tomography models
448 showed significantly slow shear wave speeds in the upper mantle beneath the
449 Hangay Dome and its surroundings (e.g., Tiberi et al., 2008; Chen et al.,
450 2015a; Comeau et al., 2018; He et al., 2019; Wu et al., 2021; Feng, 2021;
451 Wang et al., 2022; Huang and Zhao, 2022).

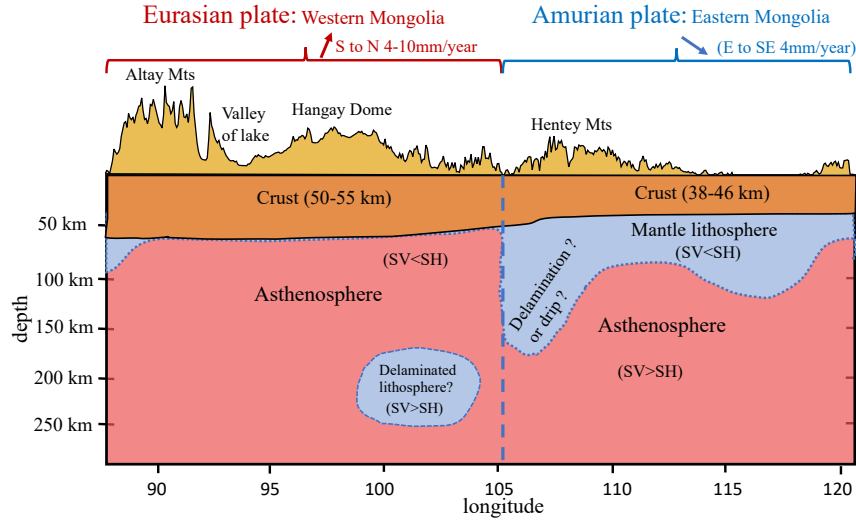


Figure 9: Schematic illustration of major structural features of our shear wave model across Mongolia (west-east cross section).

Chen et al. (2015a) found a large-scale low-speed volume in the upper mantle beneath the Hangay Dome, the Khovsgol rift system, parts of the Gobi-Altay Mountains, and the Sayan Mountains in the depth range from 50 to 90 km, although their data set lacks local seismic data in Mongolia. With low V_s (V_{sv}) of less than 4.2 km/s, they proposed that partial melting might spread over the area beneath the Hangay Dome and its environs. However, the recent V_s model by Feng (2021), who employed more extensive local data sets in this region, demonstrated that the partial melting zones are distributed not directly beneath the Hangay Dome. The partial melting and convective loss of the lithosphere may result in the uplift of Hangay Dome and may cause such low-speed anomalies. Recent P-wave tomography by Huang and Zhao (2022) suggested a velocity discontinuity at a depth of around 250

464 km, indicating that the lithosphere beneath the Hangay Dome may have
465 been delaminated (Zhao et al., 2021).

466 Numerical experiments by Elkins-Tanton (2005) on continental delam-
467 ination suggested the necessity of ductile mid-lithosphere to allow delami-
468 nation, implying that the delamination can occur in regions that have ex-
469 perience high heat flow from volcanism or mantle upwelling. Based on
470 thermo-mechanical numerical models incorporating geological, geochemical,
471 and geophysical data, Comeau et al. (2021) have investigated the conditions
472 for lithospheric removal by delaminations. They have found that central
473 Mongolia satisfied the conditions for lithospheric delamination, supported by
474 lines of evidence such as the high surface and dome-shaped topography, thin
475 lithosphere, and elevated temperature at the crust-mantle interface. These
476 findings suggest that mechanical delamination or thermal processes may be
477 to blame for the lithosphere beneath the Hangay Dome being significantly
478 weaker than the surrounding regions (Fullea et al., 2012).

479 Anomalous low velocity beneath the Hangay Dome in our model is con-
480 sistent with recent results by Feng (2021), showing low-velocity anomalies
481 down to about 180 km depth, mainly beneath the northeast of the Hangay
482 Dome, Khanuy Gol. A low-velocity region can also be seen in the upper
483 mantle beneath the Khovsgol rift to the north. The Hangay Dome is lain by
484 weak high-velocity anomalies around 200 km depths, which may represent
485 the remnant of delaminated lithosphere (e.g., Comeau et al., 2021; Huang and
486 Zhao, 2022). Our model suggests a similar high-velocity anomaly at depths
487 of around 200 km, although its location is slightly shifted to the south, not
488 right beneath the Hangay Dome (Figure S19 (d-f)).

489 The radial anisotropy maps (Figure S17) show anomalously weak re-
 490 gions with slower S wave speeds with significant positive radial anisotropy
 491 ($SH > SV$), particularly at depths of about 70–150 km, near the Hangay Dome
 492 and on the northeastern side of the Hangay Mountains, Khanuy Gol. This
 493 anomalous radial anisotropy accompanies slower SV wave speed, which can
 494 be seen beneath the Hangay Mountains down to 150 km depth. Such features
 495 may indicate the presence of finely layered or laminated heterogeneity, possi-
 496 bly including partially molten layers, which can generate significant positive
 497 radial anisotropy (e.g., Aki, 1968). Thus, our results may suggest that the
 498 Hangay Dome may be formed by oblique mantle upwelling from the north-
 499 east of the dome, accompanying large-scale partially molten layers in the top
 500 150 km depth, as indicated by Chen et al. (2015a) and Feng (2021).

501 *5.3. Eastern Mongolia: Amurian plate and its western boundary*

502 Zonenshain and Savostin (1981) proposed the "Amurian plate" cover-
 503 ing eastern Mongolia, north China, and southeastern Russia in the exten-
 504 sional areas southeast of Lake Baikal. The Amurian plate and its geometrical
 505 boundary in East Asia have been studied extensively using space geodetic
 506 observations (e.g., Takahashi et al., 1999; Heki et al., 1999; Jin, 2013), a six-
 507 plate analysis of earthquake slip vectors and NUVEL-1 data (Wei and Seno,
 508 2011), kinematics of the active faults (Sankov et al., 2022), and topography
 509 and seismicity (e.g., Bird, 2003). The southernmost edge of the Amurian
 510 plate is unclear compared to other areas. Heki et al. (1999) suggested that
 511 the south boundary of the Amurian Plate may be the Qinling fault because it
 512 is consistent with the Euler vector and predicts left-lateral movement along
 513 its boundary with the South China block. However, Jin (2013) defined the

514 tectonic boundary between the North China and Amurian plates as the Yin
515 Shan-Yan Shan Mountain belts with about 2.4 mm/yr extension. Because
516 of the sparse and limited data, these investigations of tectonics in this region
517 are inconclusive. Thus, the existence of the Amurian plate and its boundary
518 geometry remains debatable.

519 Our anisotropic S wave model provides new insights into the local tec-
520 tonic features of the eastern Mongolia region. Owing to a large number of
521 local broadband seismic stations in Mongolia, our new 3-D model shows dis-
522 tinct lateral variations near the expected boundary between the Eurasian
523 and Amurian plates (Figures 7 and 8), especially near the northern and
524 western edges of the Amurian plate. However, the southern border of the
525 Amurian plates in China is unclear due to the limited station coverage in
526 the current study. The arrows in Figure 7 (a) show the relative plate mo-
527 tion; the Indian plate moves northward at a rate of about 44 mm/year, the
528 Pacific, Okhotsk, and Philippine Sea plates move northeastward at about 93
529 mm/year, 84 mm/year and 67 mm/year, respectively, and the Amurian plate
530 moves southeastward at about 5 mm/year, for the fixed Eurasian plate based
531 on the MORVEL plate model (DeMets et al., 2010). The GPS measurements
532 in Mongolia by Calais et al. (2003) are displayed with black arrows in Fig
533 7 (a). In western Mongolia, we can see northward shortening in the Altay
534 area, which varies from 10 mm/year in the south to 4 mm/year in the north.
535 However, central and eastern Mongolia moves eastward or southeastward at
536 a rate of about 4 mm/year.

537 In the cross sections of Figure 7 (e, f), we can see clear velocity contrasts
538 between the Eurasian and Amurian plates, especially at the western and

539 northern boundaries. The lateral variations of the S wave model at 70 km
540 depth (Figure 8 (a)) show slow velocities in seismically active regions in
541 western Mongolia (1964 – 2023 $M_l \geq 3.5$) and fast velocities in stable eastern
542 Mongolia, which is likely to reflect the tectonic and structural differences
543 between the two plates. Based on the observed velocity contrast in our
544 model and local seismic activities, the western border of the Amurian plate
545 in southern Mongolia may be located to the west about 2 degrees from the
546 expected boundary by Bird (2003).

547 The dipping fast anomaly seen along the western border of the Amurian
548 plate extends to about 180 km depth (Figure 8), which may manifest under-
549 going delamination or dripping of the lithospheric mantle (Elkins-Tanton,
550 2005; West et al., 2009; Bajolet et al., 2012). The slow anomaly in the as-
551 thenosphere beneath the Hentey Mountains extends wider areas in eastern
552 Mongolia (Figures 8 and 9 and LV3 in Figure S21), which may represent
553 the small-scale mantle convection beneath this region that may promote the
554 lithospheric delamination in this area. Note that although our 3-D model well
555 constrains the large-scale ($> 2^\circ$) upper mantle structure below 60 km depth,
556 the shallower structure, including the crust, cannot be fully constrained due
557 to the limited vertical resolution of the dispersion data used in this study.
558 Also, the long-wavelength surface waves tend to blur the lithosphere images,
559 limiting the lateral resolution of surface wave tomography. Additional seis-
560 mic data, such as ambient noises and H/V ratios of Rayleigh waves, may
561 help constrain the shallower structure. Moreover, body-wave travel times
562 from local and teleseismic events will also help in higher-resolution images
563 of mantle structure. Such further seismological constraints will enable us

564 to clarify more detailed tectonic and dynamics processes in the enigmatic
565 western border of the Amurian plate.

566 **6. Conclusions**

567 We constructed a new radially anisotropic 3-D S-wave model in and
568 around Mongolian regions from multi-mode surface waves. By combining
569 broadband seismograms from the permanent and temporary seismic networks
570 in Mongolia as well as neighboring GSN, PASSCAL, and NECESSArray sta-
571 tions, we could obtain the high-resolution S wave model under the whole
572 areas of Mongolia, which provides new insight into large-scale tectonics of
573 the Mongolian region, including the western border of the Amurian plate.
574 The main conclusions of the current work can be summarized as follows.

- 575 1. S-wave speeds in the upper mantle beneath Mongolia are generally
576 slower in the tectonically active west and faster in the stable east above
577 100 km depth. The significant velocity contrast between western and
578 eastern Mongolia may reflect the boundary between the Eurasian and
579 Amurian plates.
- 580 2. In western Mongolia, two major low-velocity anomalies are found be-
581 neath the northern Altay Mountains and the Hangay Dome. The for-
582 mer persists to 300 km depth, which may relate to the northward move-
583 ment of Asian blocks due to the India-Asia collision. The latter con-
584 tinues down to 180 km depth beneath the Hangay Dome, particularly
585 Khanuy Gol in the northeast of the Hangay area, which might reflect
586 oblique upwelling.

- 587 3. In eastern Mongolia, located in the western Amurian plate, high veloc-
588 ities in the upper mantle suggest the relatively thicker lithosphere in
589 the middle Gobi. The dipping fast anomaly along the Amurian plate
590 boundary may indicate the delaminating or dripping lithosphere, which
591 can be promoted by the small-scale mantle convection represented by
592 low-velocity anomalies in the asthenosphere beneath the Hentey Moun-
593 tains.
- 594 4. The new 3-D S-wave model exhibits significant velocity contrast be-
595 tween the Eurasian and Amurian plates and structural differences in
596 the underlying upper mantle, implying the differential plate motions in
597 eastern and western Mongolia can be related to such structural varia-
598 tions and local mantle dynamics.

599 **Data Availability**

600 The majority of seismograms used in this study are available from IRIS
601 Data Management Center (<https://ds.iris.edu/ds/nodes/dmc/>). The
602 waveform data of temporary seismic networks in eastern Mongolia can be
603 available from the Earthquake Science Data Center at the Institute of Geo-
604 physics, China Earthquake Administration (<http://www.esdc.ac.cn>). The
605 waveform data of the Mongolian network are available by applying to the
606 Institute of Astronomy and Geophysics, the Mongolian Academy of Sciences
607 (iag@iag.ac.mn). The seismic events displayed in Figure 3 are downloaded
608 from the USGS database ([https://earthquake.usgs.gov/earthquakes/](https://earthquake.usgs.gov/earthquakes/search/)
609 [search/](#)). The 3-D S wave model used in this study is available from a
610 repository (<http://dx.doi.org/10.13140/RG.2.2.19423.43686>).

611 Acknowledgments

612 We thank all who helped collect the seismic data used in this study.
613 We appreciate the Institute of Astronomy and Geophysics of the Mongolian
614 Academy of Sciences and the IRIS Data Management Center for provid-
615 ing seismic waveform data. This study was partly supported by JDS (The
616 Project for Human Resource Development Scholarship by Japanese Grant
617 Aid) grant and JSPS KAKENHI Grant Numbers 20K04096 and 23K03539
618 to KY.

619 References

- 620 Aki, K., 1968. Seismological evidences for the existence of soft thin layers
621 in the upper mantle under Japan. *Journal of Geophysical Research* 73,
622 585–594. doi:10.1029/jb073i002p00585.
- 623 Bajolet, F., Galeano, J., Funiciello, F., Moroni, M., Negredo, A.M., Fac-
624 cenna, C., 2012. Continental delamination: Insights from laboratory mod-
625 els. *Geochemistry, Geophysics, Geosystems* 13. URL: [http://doi.wiley.](http://doi.wiley.com/10.1029/2011GC003896)
626 [com/10.1029/2011GC003896](http://doi.wiley.com/10.1029/2011GC003896), doi:10.1029/2011GC003896.
- 627 Barry, T.L., Kent, R.W., 1998. Cenozoic magmatism in Mongolia and the
628 origin of central and east Asian basalts, in: Martin F.J. Folower, Sun-Lin
629 Chung, Ching-Hua Lo, Tung-Yi Lee (Eds.), *Mantle Dynamics and Plate*
630 *Interactions in East Asia*. American Geophysical Union, Washington D.C.,
631 pp. 347–364. URL: [http://www.agu.org/books/gd/v027/GD027p0347/](http://www.agu.org/books/gd/v027/GD027p0347/GD027p0347.shtml)
632 [GD027p0347.shtml](http://www.agu.org/books/gd/v027/GD027p0347/GD027p0347.shtml).

633 Barry, T.L., Saunders, A.D., Kempton, P.D., Windley, B.F., Pringle, M.S.,
634 Dorjnamjaa, D., Saandar, S., 2003. Petrogenesis of Cenozoic basalts from
635 Mongolia: Evidence for the role of asthenospheric versus metasomatized
636 lithospheric mantle sources. *Journal of Petrology* 44, 55–91. doi:10.1093/
637 *petrology*/44.1.55.

638 Bird, P., 2003. An updated digital model of plate boundaries. *Geochemistry,*
639 *Geophysics, Geosystems* 4, 1027. doi:10.1029/2001GC000252.

640 Calais, E., Vergnolle, M., San'kov, V., Lukhnev, A., Miroshnitchenko, A.,
641 Amarjargal, S., Déverchère, J., 2003. GPS measurements of crustal defor-
642 mation in the Baikal-Mongolia area (1994-2002): Implications for current
643 kinematics of Asia. *Journal of Geophysical Research: Solid Earth* 108,
644 2501. doi:10.1029/2002jb002373.

645 Chen, M., Niu, F., Liu, Q., Tromp, J., 2015a. Mantle-driven uplift of Hangai
646 Dome: New seismic constraints from adjoint tomography. *Geophysical*
647 *Research Letters* 42, 6967–6974. doi:10.1002/2015GL065018.

648 Chen, M., Niu, F., Liu, Q., Tromp, J., Zheng, X., 2015b. Multiparameter
649 adjoint tomography of the crust and upper mantle beneath East Asia: 1.
650 Model construction and comparisons. *Journal of Geophysical Research:*
651 *Solid Earth* 120, 1762–1786. doi:10.1002/2014JB011638.

652 Comeau, M.J., Käufl, J.S., Becken, M., Kuvshinov, A., Grayver, A.V.,
653 Kamm, J., Demberel, S., Sukhbaatar, U., Batmagnai, E., 2018. Evidence
654 for fluid and melt generation in response to an asthenospheric upwelling

655 beneath the Hangai Dome, Mongolia. *Earth and Planetary Science Letters*
656 487, 201–209. doi:10.1016/j.epsl.2018.02.007.

657 Comeau, M.J., Stein, C., Becken, M., Hansen, U., 2021. Geodynamic
658 Modeling of Lithospheric Removal and Surface Deformation: Applica-
659 tion to Intraplate Uplift in Central Mongolia. *Journal of Geophysical Re-*
660 *search: Solid Earth* 126, e2020JB021304 – 26. URL: [https://agupubs.](https://agupubs.onlinelibrary.wiley.com/doi/full/10.1029/2020JB021304)
661 [onlinelibrary.wiley.com/doi/full/10.1029/2020JB021304](https://agupubs.onlinelibrary.wiley.com/doi/full/10.1029/2020JB021304), doi:10.
662 1029/2020JB021304.

663 Cunningham, W.D., 2001. Cenozoic normal faulting and regional doming in
664 the southern Hangay region, Central Mongolia: Implications for the origin
665 of the Baikal rift province. *Tectonophysics* 331, 389–411. URL: [www.](http://www.elsevier.com/locate/tecto)
666 [elsevier.com/locate/tecto](http://www.elsevier.com/locate/tecto), doi:10.1016/s0040-1951(00)00228-6.

667 DeMets, C., Gordon, R.G., Argus, D.F., 2010. Geologically current plate
668 motions. *Geophysical Journal International* 181, 1–80. doi:10.1111/j.
669 1365-246X.2009.04491.x.

670 Dziewonski, A.M., Anderson, D.L., 1981. Preliminary reference Earth model.
671 *Physics of the Earth and Planetary Interiors* 25, 297–356. doi:10.1016/
672 0031-9201(81)90046-7.

673 Ekström, G., 2011. A global model of Love and Rayleigh surface wave dis-
674 persion and anisotropy, 25-250s. *Geophysical Journal International* 187,
675 1668–1686. doi:10.1111/j.1365-246X.2011.05225.x.

676 Ekström, G., Nettles, M., Dziewoński, A.M., 2012. The global CMT project
677 2004-2010: Centroid-moment tensors for 13,017 earthquakes. *Physics of*

678 the Earth and Planetary Interiors 200-201, 1–9. doi:10.1016/j.pepi.
679 2012.04.002.

680 Elkins-Tanton, L.T., 2005. Continental magmatism caused by lithospheric
681 delamination, in: Foulger, G.R., Natland, J.H., Presnall, D.C., Ander-
682 son, D.L. (Eds.), Plates, plumes and paradigms. Geological Society of
683 America. volume 388, pp. 449–461. URL: [https://doi.org/10.1130/](https://doi.org/10.1130/0-8137-2388-4.449)
684 [0-8137-2388-4.449](https://doi.org/10.1130/0-8137-2388-4.449), doi:10.1130/0-8137-2388-4.449.

685 Erdenesaihan, G., Ishiwatari, A., Orolmaa, D., Arai, S., Tamura, A.,
686 2013. Middle paleozoic greenstones of the Hangay region, central Mon-
687 golia: Remnants of an accreted oceanic plateau and forearc magma-
688 tism. Journal of Mineralogical and Petrological Sciences 108, 303–325.
689 doi:10.2465/jmps.130409.

690 Feng, L., 2021. High-Resolution Crustal and Uppermost Mantle Struc-
691 ture Beneath Central Mongolia From Rayleigh Waves and Receiver Func-
692 tions. Journal of Geophysical Research: Solid Earth 126. doi:10.1029/
693 2020JB021161.

694 Fullea, J., Lebedev, S., Agius, M.R., Jones, A.G., Afonso, J.C., 2012.
695 Lithospheric structure in the Baikal-central Mongolia region from inte-
696 grated geophysical-petrological inversion of surface-wave data and topo-
697 graphic elevation. Geochemistry, Geophysics, Geosystems 13, n/a–n/a.
698 doi:10.1029/2012GC004138.

699 Global Volcanism Program, 2023. [Database] Volcanoes of the World (v.
700 5.1.0; 9 Jun 2023). Distributed by Smithsonian Institution, compiled by

701 Venzke, E. URL: <https://doi.org/10.5479/si.GVP.V0TW5-2023.5.1>,
702 doi:10.5479/si.GVP.V0TW5-2023.5.1.

703 Gung, Y., Panning, M., Romanowicz, B., 2003. Global anisotropy and the
704 thickness of continents. *Nature* 422, 707–711. URL: <http://www.nature.com/doi/finder/10.1038/nature01559>, doi:10.1038/nature01559.
705

706 Hao, M., Li, Y., Zhuang, W., 2019. Crustal movement and strain distribution
707 in East Asia revealed by GPS observations. *Scientific Reports* 9. doi:10.
708 1038/s41598-019-53306-y.

709 He, J., Li, Y., Sandvol, E., Wu, Q., Du, G., Zhang, R., Yu, D., Liu, H., Lei,
710 J., Huang, J., 2019. Tomographic Pn Velocity and Anisotropy Structure
711 in Mongolia and the Adjacent Regions. *Journal of Geophysical Research:*
712 *Solid Earth* 124, 3662–3679. doi:10.1029/2018JB016440.

713 He, J., Wu, Q., Sandvol, E., Ni, J., Gallegos, A., Gao, M., Ulziibat, M.,
714 Demberel, S., 2016. The crustal structure of south central Mongolia using
715 receiver functions. *Tectonics* 35, 1392–1403. doi:10.1002/2015TC004027.

716 Heki, K., Miyazaki, S.N., Takahashi, H., Kasahara, M., Kimata, F., Miura,
717 S., Vasilenko, N.F., Ivashchenko, A., An, K.D., 1999. The amurian plate
718 motion and current plate kinematics in eastern Asia. *Journal of Geophys-*
719 *ical Research: Solid Earth* 104, 29147–29155. doi:10.1029/1999jb900295.

720 Huang, J., Zhao, D., 2006. High-resolution mantle tomography of China and
721 surrounding regions. *Journal of Geophysical Research: Solid Earth* 111.
722 doi:10.1029/2005JB004066.

723 Huang, Z., Zhao, D., 2022. Seismotectonics of Mongolia and Baikal Rift Zone
 724 Controlled by Lithospheric Structures. *Geophysical Research Letters* 49.
 725 doi:10.1029/2022GL099525.

726 Hunt, A.C., Parkinson, I.J., Harris, N.B., Barry, T.L., Rogers, N.W.,
 727 Yondon, M., 2012. Cenozoic volcanism on the Hangai Dome, Central
 728 Mongolia: Geochemical evidence for changing melt sources and implica-
 729 tions for mechanisms of melting. *Journal of Petrology* 53, 1913–1942.
 730 doi:10.1093/petrology/egs038.

731 Jin, S., 2013. GNSS Observations of Crustal Deformation: A Case Study in
 732 East Asia, in: *Geodetic Sciences - Observations, Modeling and Applica-*
 733 *tions*. IntechOpen, pp. 267–284. doi:10.5772/51536.

734 Kennett, B.L.N., Yoshizawa, K., 2002. A reappraisal of regional surface wave
 735 tomography. *Geophysical Journal International* 150, 37–44. doi:10.1046/
 736 j.1365-246X.2002.01682.x.

737 Khutorskoy, M., Yarmoluk, V., 1989. Heat flow, structure and evolution of
 738 the lithosphere of Mongolia. *Tectonophysics* 164, 315–322. URL: [https://](https://linkinghub.elsevier.com/retrieve/pii/0040195189900243)
 739 linkinghub.elsevier.com/retrieve/pii/0040195189900243, doi:10.
 740 1016/0040-1951(89)90024-3.

741 Laske, G., Masters, G., Ma, Z., Pasyanos, M., 2013. Update on CRUST1.0—
 742 A 1-degree global model of Earth’s crust. *EGU General Assembly 2013*
 743 15, 2658. URL: [http://meetingorganizer.copernicus.org/EGU2013/](http://meetingorganizer.copernicus.org/EGU2013/EGU2013-2658.pdf)
 744 [EGU2013-2658.pdf](http://meetingorganizer.copernicus.org/EGU2013/EGU2013-2658.pdf).

- 745 Li, M., Song, X., Li, J., Bao, X., 2022. Crust and upper mantle struc-
746 ture of East Asia from ambient noise and earthquake surface wave to-
747 mography. *Earthquake Science* 35, 71–92. URL: [https://linkinghub.](https://linkinghub.elsevier.com/retrieve/pii/S1674451922000349)
748 [elsevier.com/retrieve/pii/S1674451922000349](https://linkinghub.elsevier.com/retrieve/pii/S1674451922000349), doi:10.1016/j.eqs.
749 2022.05.004.
- 750 McDannell, K.T., Zeitler, P.K., Idleman, B.D., 2018. Relict Topography
751 Within the Hangay Mountains in Central Mongolia: Quantifying Long-
752 Term Exhumation and Relief Change in an Old Landscape. *Tectonics* 37, 2531–2558. URL: [https://onlinelibrary.wiley.com/doi/10.](https://onlinelibrary.wiley.com/doi/10.1029/2017TC004682)
753 [1029/2017TC004682](https://onlinelibrary.wiley.com/doi/10.1029/2017TC004682), doi:10.1029/2017TC004682.
- 755 Meltzer, A., Stachnik, J.C., Sodnomsambuu, D., Munkhuu, U., Tsagaan,
756 B., Dashdondog, M., Russo, R., 2019. The central Mongolia seismic
757 experiment: Multiple applications of temporary broadband seis-
758 mic arrays. *Seismological Research Letters* 90, 1364–1376. URL:
759 [https://pubs.geoscienceworld.org/ssa/srl/article/90/3/1364/](https://pubs.geoscienceworld.org/ssa/srl/article/90/3/1364/569839/The-Central-Mongolia-Seismic-Experiment-Multiple)
760 [569839/The-Central-Mongolia-Seismic-Experiment-Multiple](https://pubs.geoscienceworld.org/ssa/srl/article/90/3/1364/569839/The-Central-Mongolia-Seismic-Experiment-Multiple),
761 doi:10.1785/0220180360.
- 762 Meng, Q.R., Hu, J.M., Jin, J.Q., Zhang, Y., Xu, D.F., 2003. Tectonics of
763 the late Mesozoic wide extensional basin system in the China-Mongolia
764 border region. *Basin Research* 15, 397–415. doi:10.1046/j.1365-2117.
765 2003.00209.x.
- 766 Molnar, P., Tapponnier, P., 1975. Cenozoic tectonics of Asia: Effects of a
767 continental collision. *Science* 189, 419–426. doi:10.1126/science.189.
768 4201.419.

- 769 Montagner, J.P., Anderson, D.L., 1989. Petrological constraints on seis-
770 mic anisotropy. *Physics of the Earth and Planetary Interiors* 54, 82–105.
771 doi:10.1016/0031-9201(89)90189-1.
- 772 Nataf, H.C., Ricard, Y., 1996. 3SMAC: An a priori tomographic model
773 of the upper mantle based on geophysical modeling. *Physics of the Earth*
774 *and Planetary Interiors* 95, 101–122. URL: [http://dx.doi.org/10.1016/](http://dx.doi.org/10.1016/0031-9201(95)03105-7)
775 [0031-9201\(95\)03105-7](http://dx.doi.org/10.1016/0031-9201(95)03105-7), doi:10.1016/0031-9201(95)03105-7.
- 776 Pan, J.T., Wu, Q., Li, Y., Yu, D.X., Gao, M., Ulziibat, M., Demberel, S.,
777 2015. Ambient Noise Tomography in Central-South Mongolia. *Chinese*
778 *Journal of Geophysics* 58, 3009–3022. doi:10.6038/cjg20150832.
- 779 Panning, M., Romanowicz, B., 2006. A three-dimensional radially anisotropic
780 model of shear velocity in the whole mantle. *Geophysical Journal Interna-*
781 *tional* 167, 361–379. doi:10.1111/j.1365-246X.2006.03100.x.
- 782 Petit, C., Déverchère, J., Calais, E., San’kov, V., Fairhead, D., 2002. Deep
783 structure and mechanical behavior of the lithosphere in the Hangai-Hövsgöl
784 region, Mongolia: New constraints from gravity modeling. *Earth and*
785 *Planetary Science Letters* 197, 133–149. doi:10.1016/S0012-821X(02)
786 [00470-3](https://doi.org/10.1016/S0012-821X(02)00470-3).
- 787 Petit, C., Tiberi, C., Deschamps, A., Déverchère, J., 2008. Teleseismic travel-
788 times, topography and the lithospheric structure across central Mongolia.
789 *Geophysical Research Letters* 35. doi:10.1029/2008GL033993.
- 790 Ritzwoller, M.H., Shapiro, N.M., Barmin, M.P., Levshin, A.L., 2002. Global

791 surface wave diffraction tomography. *Journal of Geophysical Research:*
792 *Solid Earth* 107, 4–1. doi:10.1029/2002jb001777.

793 Sambridge, M., 1999. Geophysical inversion with a neighbourhood algorithm
794 - I. Searching a parameter space. *Geophysical Journal International* 138,
795 479–494. doi:10.1046/j.1365-246X.1999.00876.x.

796 Sankov, V.A., Parfeevets, A.V., Miroshnitchenko, A.I., Sankov, A.V., Bayas-
797 galan, A., Demberel, S., 2022. Active faulting along the western boundary
798 of the Amur plate (territory of Mongolia). *Earth Science Frontiers* 29,
799 245–265. doi:10.13745/j.esf.sf.2021.12.16.

800 Takahashi, H., Kasahara, M., Kimata, F., Miura, S., Heki, K., Seno,
801 T., Kato, T., Vasilenko, N., Ivashchenko, A., Bahtiarov, V., Levin, V.,
802 Gordeev, E., Korchagin, F., Gerasimenko, M., 1999. Velocity field of
803 around the Sea of Okhotsk and Sea of Japan regions determined from
804 a new continuous GPS network data. *Geophysical Research Letters* 26,
805 2533–2536. doi:10.1029/1999GL900565.

806 Tao, K., Grand, S.P., Niu, F., 2018. Seismic Structure of the Upper
807 Mantle Beneath Eastern Asia From Full Waveform Seismic Tomogra-
808 phy. *Geochemistry, Geophysics, Geosystems* 19, 2732–2763. doi:10.1029/
809 2018GC007460.

810 Tarantola, A., Valette, B., 1982. Generalized nonlinear inverse problems
811 solved using the least squares criterion. *Reviews of Geophysics* 20, 219–
812 232. doi:10.1029/RG020i002p00219.

- 813 Tiberi, C., Deschamps, A., Déverchère, J., Petit, C., Perrot, J., Ap-
 814 priou, D., Mordvinova, V., Dugaarma, T., Ulzibaat, M., Artemiev, A.A.,
 815 2008. Asthenospheric imprints on the lithosphere in Central Mongolia
 816 and Southern Siberia from a joint inversion of gravity and seismology
 817 (MOBAL experiment). *Geophysical Journal International* 175, 1283–1297.
 818 doi:10.1111/j.1365-246X.2008.03947.x.
- 819 Walker, R.T., Nissen, E., Molodtsov, E., Bayasgalan, A., 2007. Reinterpretation
 820 of the active faulting in central Mongolia. *Geology* 35, 759–762. doi:10.
 821 1130/G23716A.1.
- 822 Wang, X., Wu, H., Wang, H., Wu, B., Huang, Z., 2022. Rayleigh wave
 823 tomography of central and southern Mongolia. *Tectonophysics* 836. doi:10.
 824 1016/j.tecto.2022.229426.
- 825 Wei, D., Seno, T., 2011. Determination of the Amurian plate motion, in:
 826 *Mantle Dynamics and Plate Interactions in East Asia*. Washington. vol-
 827 ume 27, pp. 337–346. doi:10.1029/gd027p0337.
- 828 Wei, W., Xu, J., Zhao, D., Shi, Y., 2012. East Asia mantle tomography: New
 829 insight into plate subduction and intraplate volcanism. *Journal of Asian*
 830 *Earth Sciences* 60, 88–103. doi:10.1016/j.jseaes.2012.08.001.
- 831 West, J.D., Fouch, M.J., Roth, J.B., Elkins-Tanton, L.T., 2009. Vertical man-
 832 tle flow associated with a lithospheric drip beneath the Great Basin. *Nature*
 833 *Geoscience* 2, 439–444. URL: [https://www.nature.com/articles/](https://www.nature.com/articles/ngeo526)
 834 [ngeo526](https://www.nature.com/articles/ngeo526), doi:10.1038/ngeo526.

- 835 Windley, B.F., Alexeiev, D., Xiao, W., Kröner, A., Badarch, G., 2007. Tec-
 836 tonic models for accretion of the Central Asian Orogenic Belt. *Journal of*
 837 *the Geological Society* 164, 31–47. doi:10.1144/0016-76492006-022.
- 838 Windley, B.F., Allen, M.B., 1993. Mongolian Plateau: evidence
 839 for a late Cenozoic mantle plume under central Asia. *Geology*
 840 21, 295–298. URL: [http://pubs.geoscienceworld.org/gsa/geology/](http://pubs.geoscienceworld.org/gsa/geology/article-pdf/21/4/295/3514255/i0091-7613-21-4-295.pdf)
 841 [article-pdf/21/4/295/3514255/i0091-7613-21-4-295.pdf](http://pubs.geoscienceworld.org/gsa/geology/article-pdf/21/4/295/3514255/i0091-7613-21-4-295.pdf), doi:10.
 842 1130/0091-7613(1993)021<0295:MPEFAL>2.3.CO;2.
- 843 Witek, M., Chang, S.J., Lim, D.Y., Ning, S., Ning, J., 2021. Radial
 844 Anisotropy in East Asia From Multimode Surface Wave Tomography. *Jour-*
 845 *nal of Geophysical Research: Solid Earth* 126. doi:10.1029/2020JB021201.
- 846 Wu, H., Huang, Z., Zhao, D., 2021. Deep structure beneath the southwestern
 847 flank of the Baikal rift zone and adjacent areas. *Physics of the Earth and*
 848 *Planetary Interiors* 310. doi:10.1016/j.pepi.2020.106616.
- 849 Yoshizawa, K., 2014. Radially anisotropic 3-D shear wave structure of the
 850 Australian lithosphere and asthenosphere from multi-mode surface waves.
 851 *Physics of the Earth and Planetary Interiors* 235, 33–48. doi:10.1016/j.
 852 [pepi.2014.07.008](https://doi.org/10.1016/j.pepi.2014.07.008).
- 853 Yoshizawa, K., Ekström, G., 2010. Automated multimode phase speed mea-
 854 surements for high-resolution regional-scale tomography: Application to
 855 North America. *Geophysical Journal International* 183. doi:10.1111/j.
 856 1365-246X.2010.04814.x.

- 857 Yoshizawa, K., Kennett, B.L.N., 2002a. Determination of the influence zone
858 for surface wave paths. *Geophysical Journal International* 149, 440–453.
859 doi:10.1046/j.1365-246X.2002.01659.x.
- 860 Yoshizawa, K., Kennett, B.L.N., 2002b. Non-linear waveform inversion
861 for surface waves with a neighbourhood algorithm-application to multi-
862 mode dispersion measurements. *Geophysical Journal International* 149,
863 118–133. URL: [https://academic.oup.com/gji/article/149/1/118/](https://academic.oup.com/gji/article/149/1/118/620393)
864 620393, doi:10.1046/j.1365-246X.2002.01634.x.
- 865 Yoshizawa, K., Kennett, B.L.N., 2004. Multimode surface wave tomogra-
866 phy for the Australian region using a three-stage approach incorporating
867 finite frequency effects. *Journal of Geophysical Research: Solid Earth* 109.
868 doi:10.1029/2002jb002254.
- 869 Yu, D.X., Wu, Q.J., Li, Y.H., Pan, J.T., Zhang, F.X., He, J., Gao, M.T.,
870 Ulziibat, M., Demberel, S., 2015. Rayleigh wave tomography of the phase
871 velocity in the central and southern Mongolia. *Acta Geophysica Sinica* 58,
872 134–142. doi:10.6038/cjg20150111.
- 873 Zhang, F., Wu, Q., Grand, S.P., Li, Y., Gao, M., Demberel, S., Ulziibat, M.,
874 Sukhbaatar, U., 2017. Seismic velocity variations beneath central Mongo-
875 lia: Evidence for upper mantle plumes? *Earth and Planetary Science Let-*
876 *ters* 459, 406–416. URL: [https://linkinghub.elsevier.com/retrieve/](https://linkinghub.elsevier.com/retrieve/pii/S0012821X16306872)
877 [pii/S0012821X16306872](https://linkinghub.elsevier.com/retrieve/pii/S0012821X16306872), doi:10.1016/j.epsl.2016.11.053.
- 878 Zhao, H., Wang, P., Huang, Z., 2021. Lithospheric structures beneath the
879 western Mongolian Plateau: Insight from S wave receiver function. *Jour-*

880 nal of Asian Earth Sciences 212, 104733. doi:10.1016/j.jseaes.2021.
 881 104733.

882 Zonenshain, L.P., Savostin, L.A., 1981. Geodynamics of the Baikal rift
 883 zone and plate tectonics of Asia. Tectonophysics 76, 1–45. doi:10.1016/
 884 0040-1951(81)90251-1.

885 Zorin, Y.A., Novoselova, M.R., Turutanov, E.K., Kozhevnikov, V.M.,
 886 1990. Structure of the lithosphere of the Mongolian-Siberian moun-
 887 tainous province. Journal of Geodynamics 11, 327–342. doi:10.1016/
 888 0264-3707(90)90015-M.

889 Zorin, Y.A., Turutanov, E.K., Kozhevnikov, V.M., Rasskazov, S.V., Ivanov,
 890 A.V., 2006. Cenozoic upper mantle plumes in East Siberia and Central
 891 Mongolia and subduction of the Pacific Plate. Doklady Earth Sciences
 892 409, 723–726. doi:10.1134/S1028334X06050096.